AC electrohydrodynamic instabilities in thin liquid films

SCOTT A. ROBERTS AND SATISH KUMAR†

Department of Chemical Engineering and Materials Science, University of Minnesota, Minneapolis,
Minnesota 55455, USA

When DC electric fields are applied to a thin liquid film, the interface may become unstable and form a series of pillars. In this paper, we apply lubrication theory to examine the possibility of using AC electric fields to exert further control over the size and shape of the pillars. For perfect dielectric films, linear stability analysis shows that the influence of an AC field can be understood by considering an effective DC field. For leaky dielectric films, Floquet theory is applied to carry out the linear stability analysis, and it reveals that high frequencies may be used to inhibit the accumulation of interfacial free charge, leading to a lowering of growth rates and wavenumbers. Nonlinear simulations confirm the results of the linear stability analysis while also uncovering additional mechanisms for tuning overall pillar height and width. The results presented here may be of interest for the controlled creation of surface topographical features in applications such as patterned coatings and microelectronics.

1. Introduction

Thin polymer films are ubiquitous in modern technologies, ranging from coatings (Assender, Bliznyuk & Porfyrakis 2002; Harrison *et al.* 2004) to plastic electronics (DeAro *et al.* 1997; Nabetani *et al.* 2001) to biomaterials (Curtis & Wilkinson 1997; Ranucci & Moghe 2001; Conti *et al.* 2002; Tsai *et al.* 2004). While perfectly flat coatings may be desirable in some applications, other uses require the creation of regular surface patterns (Assender *et al.* 2002). Controlling the surface topography of thin polymer films becomes more difficult as the films become thinner and the desired topography becomes smaller.

In the late 1990s, Chou and co-workers (Chou & Zhuang 1999; Chou, Zhuang & Guo 1999) discovered that thin polymer films may form pillars when subjected to a vertical electric field. In this process, known as lithographically induced self-assembly (LISA), a polymer melt is cast on a silicon substrate and sandwiched underneath a top mask, leaving a small air gap between the polymer and the mask. When the polymer is heated above its glass transition temperature, an electric field arises between the substrate and the mask, and the interface between the air and polymer film deforms into an array of pillars. This electric field is created by induced charges between the polymer and the mask. These features can be locked in by then cooling to below the glass transition temperature, yielding a tightly packed, regular array of glassy polymer pillars. Initial experiments by Chou & Zhuang (1999) were able to generate

† Email address for correspondence: kumar@cems.umn.edu

pillars with diameters of 1 µm and a pillar height-to-width ratio of 0.5. These pillars could serve as topographical features for the previously mentioned applications.

Only after the experiments of Chou and co-workers did researchers focus on controlling these patterns using externally applied electric fields. Experiments using external electric fields were first performed by Schäffer *et al.* (2000, 2001) and Lin *et al.* (2001, 2002), who found that the application of an external electric field enhances the instability, leading to the formation of well-defined arrays of pillars. Smaller feature sizes were also achieved, with pillar diameters nearing 100 nm (Schäffer *et al.* 2001). Replacing the air layer with a liquid (Lin *et al.* 2001) decreases the interfacial tension, leading to a smaller pillar spacing and faster growth. Additionally, pillars may be formed into ordered gratings or concentric rings by using a coarsely patterned design on the mask, leading to features with 50 nm line widths (Lei *et al.* 2003; Deshpande *et al.* 2004). Further experiments have extended these results to a trilayer geometry, where two polymer layers are coated on the substrate rather than one (Morariu *et al.* 2003; Leach *et al.* 2005; Bandyopadhyay & Sharma 2007). This has led to even more novel structures such as hollow pillars (Dickey *et al.* 2006, 2007; Voicu, Harkema & Steiner 2006; Voicu *et al.* 2007; Lee *et al.* 2006*b*; delCampo *et al.* 2007).

Many researchers have sought to understand the above phenomena through mathematical modelling. Describing the polymer layer as a perfect dielectric material, Schäffer *et al.* (2001) and Lin *et al.* (2001) used long-wave linear stability analyses to predict how the fastest-growing wavelength depends on the film thickness and viscosity ratio. This wavelength directly correlates to the pillar spacings and widths. To improve this analysis, Pease & Russel (2002) used the leaky dielectric model, which allows for free charge at polymer interfaces. This study showed that the presence of even a very small amount of charge at the interface has a strong destabilizing influence, leading to smaller wavelengths and larger growth rates. To improve previous analyses, which used the lubrication approximation, Pease & Russel (2003) presented a generalized linear stability analysis that relaxed this approximation. They showed that as surface tension is decreased and the electric field is increased, which are the conditions needed to form the smallest pillars, the lubrication approximation fails to correctly predict pillar features. Shankar & Sharma (2004) later extended the lubrication analysis to allow the gap fluid to also be a polymer film, highlighting the importance of the viscosity and conductivity ratios in determining the pattern wavelength. More recently, Pease & Russel (2006) summarized how the distribution of interfacial charges and the tangential stresses they create have a profound impact on the pillar structure of this system.

Whereas linear stability analyses are restricted to small-amplitude perturbations, nonlinear simulations can be used to study the pillar growth process beyond this regime. Wu & Chou (2003) and Craster & Matar (2005) used one-dimensional nonlinear simulations under the lubrication approximation to investigate the growth rate and pillar-spacing characteristics of perfect dielectric (Wu & Chou 2003) and leaky dielectric (Craster & Matar 2005) fluids. Their results confirmed growth rate and wavelength trends uncovered through prior linear stability analyses. Thaokar & Kumaran (2005) used a weakly nonlinear analysis to show that the interfacial instability is subcritical for nearly all parameter values and used a boundary-element technique to study systems where the unstable wavelength is of the same order of magnitude as the initial film thickness. Two-dimensional lubrication-approximation-based simulations have also been performed, yielding insight into how various nonlinear interactions and mask shapes influence the patterns observed (Wu,

Pease & Russel 2005; Verma *et al.* 2005). Pillar configurations are consistent with those seen in experiments. Wu & Russel (2005) also studied the dynamics of the pillar formation process with simulations, showing how pillar formation begins at the edge of mask patterns and propagates inwards. Alternatively, Kim & Lu (2006) used a phase-field model to conduct three-dimensional simulations of the dynamics of this growth.

The instability generated by a DC electrostatic field is similar to that of the Rayleigh–Taylor problem, where gravitational forces can overcome the stabilizing effect of surface tension to destabilize a flat fluid interface. However, vertically oscillating a container of liquid with an effective gravity $g - a\cos(\omega t)$ can cause an instability to occur even if the mean gravity itself is stabilizing and $a < g$ (Benjamin & Ursell 1954), the so-called Faraday instability (Faraday 1831). The frequency and amplitude of oscillation can be modified to exhibit fine control over the patterns formed by the Faraday instability (Edwards & Fauve 1994; Kumar & Bajaj 1995; Topaz, Porter & Silber 2004). Because of the similarity between the Rayleigh–Taylor problem, where gravity drives the instability, and DC electrohydrodynamics (EHD), where the electric field is destabilizing, one might expect that there would be an analogue to the Faraday instability using AC EHD. This connection has been studied as far back as in the 1960s (Devitt & Melcher 1965; Reynolds 1965; Briskman & Shaidurov 1968; Yih 1968). Both Briskman & Shaidurov (1968) and Yih (1968) used stability analyses of inviscid fluids to obtain a Mathieu equation for the interfacial height, allowing calculation of the critical electric field needed to destabilize a liquid interface. Robinson *et al.* (2000, 2001, 2002) also studied how water confined in a channel and subjected to a perpendicular AC electric field can form regular projections at the water–air interface that resemble a standing wave. The properties of the AC field can be used to manipulate the behaviour of these projections, which is well described by a Mathieu equation similar to that of Yih (1968). For these instabilities, liquid inertia plays a key role, whereas for instabilities in thin films, liquid inertia is usually neglected. We also note that the use of AC fields to destabilize fluid jets has been studied both theoretically (González *et al.* 1989; González, Ramos & Castellanos 1997, 1999; González, Garcia & Castellanos 2003) and experimentally (Sato 1984; Yeo *et al.* 2004; Lee *et al.* 2006*a*), and it has been found that AC fields may be used to create smaller droplets, which is of interest for ink-jet printing. However, no studies have looked at how AC fields may be used to control thin-film pattern formation.

To summarize, DC electrostatic fields can be used to create topographical patterns on thin polymer films. Tangential stresses have been shown to play a key role in accurately modelling this phenomenon. These stresses are due to the presence of free charge at the polymer interface and are modelled by the leaky dielectric model. In studies of related systems such as jets and free water surfaces, AC electrostatic fields have been used to create instabilities not seen with DC fields and to exert further control over the behaviour of the instabilities that do exist under DC fields. Because of these successes, we believe that AC electric fields may be useful in controlling interfacial instabilities in thin liquid films. Therefore, we present in this work a theoretical study of interfacial instabilities in thin perfect dielectric and leaky dielectric films using linear stability analysis and nonlinear simulations. In §2, we present a derivation of the theoretical model appropriate for this study. Results for perfect dielectric fluids are presented in §3 and those for leaky dielectric fluids in §4. Some additional effects due to time-varying DC fields are presented in §5. The overall effect of AC and DC fields on EHD patterning is summarized in §6.
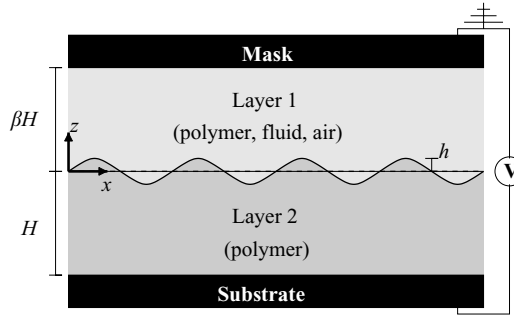
FIGURE 1. Schematic of problem geometry. Coordinates are set such that the x-direction is horizontal, the z-direction vertical, $z = 0$ is located at the initially flat interface between the two fluids and $z = h(x, t)$ is the current interface location.

2. Model

In this work, we consider a two-dimensional model of a fluid film on top of a liquid film sandwiched between two solid, impermeable, and conducting substrates of infinite horizontal extent, as illustrated in figure 1. We refer to the top substrate as the mask. The immiscible fluids are incompressible, Newtonian and are described by the leaky dielectric model (Taylor & McEwan 1965; Melcher & Warren 1966; Melcher & Smith 1969; Saville 1997). The top layer ($i = 1$) is located at $h(x, t) < z < \beta H$, and the lower layer ($i = 2$) is at $-H < z < h(x, t)$. Each layer has a constant viscosity μ_i, density ρ_i, dielectric constant ε_i and conductivity σ_i. Interfacial tension γ balances the electrostatic forces, which are due to a potential $\psi = V(t)$, maintained at the bottom substrate $z = -H$. We note that while some physical properties, such as the dielectric constant, may in general be frequency dependent (Russel, Saville & Schowalter 1989), the time scales explored in this study are well outside the region where these frequency-dependencies occur.

2.1. *Governing equations*

In the development of this model, we exploit the naturally small aspect ratios which are present, permitting the use of lubrication theory. While we recognize that Pease & Russel (2003, 2004) showed that the lubrication approximation is not valid in some situations for DC fields, we utilize it in order to more easily understand the physics at work when AC fields are used. For a detailed derivation of the leaky dielectric model, see Saville (1997).

The electrostatics in both fluids ($i = 1, 2$) are modelled by the Laplace equation for the electrostatic potential

$$\nabla^2 \psi_i = 0, \tag{2.1}$$

where the electric field is $\boldsymbol{E}_i = -\nabla \psi_i$. This description of the potential is completed by four boundary conditions. The top mask is electrically grounded and the bottom substrate is maintained at a set potential

$$\psi_1 = 0 \quad \text{at} \quad z = \beta H, \tag{2.2}$$

$$\psi_2 = V(t) \quad \text{at} \quad z = -H. \tag{2.3}$$

At the interface between the two fluids, the interfacial charge density, $q(x, t)$, is equal to the jump in the normal component of the electric field

$$q(x, t) = \| -\varepsilon_i \varepsilon_0 \nabla \psi_i \| \cdot \boldsymbol{n} \quad \text{at} \quad z = h(x, t), \tag{2.4}$$

where ε_0 is the permittivity of free space. A tangential balance of the electric field leads to equality of the potentials at the interface

$$\psi_1 = \psi_2 \quad \text{at} \quad z = h(x, t). \tag{2.5}$$

In (2.4), the jump operator denotes subtraction of the quantity evaluated in layer 2 from that evaluated in layer 1, $\|(\cdots)_i\| = (\cdots)_1 - (\cdots)_2$. We denote the normal vector pointing upwards (into layer 1) as $\boldsymbol{n}$, and $\boldsymbol{t}$ is the associated tangent vector.

Hydrodynamics in both layers are governed by the creeping flow equations

$$\nabla \cdot \boldsymbol{v}_i = 0, \tag{2.6}$$

$$\nabla \cdot \boldsymbol{T}_i = 0, \tag{2.7}$$

where $\boldsymbol{v}_i$ is the velocity field in the fluid. The total stress tensor, $\boldsymbol{T}_i$, is given by the sum of the isotropic pressure, Newtonian viscous stress, and electrical Maxwell stress tensors, the latter of which is given by

$$\boldsymbol{M}_i = \varepsilon_i \varepsilon_0 [\boldsymbol{E}_i \boldsymbol{E}_i - \tfrac{1}{2}(\boldsymbol{E}_i \cdot \boldsymbol{E}_i)\boldsymbol{\delta}], \tag{2.8}$$

where $\boldsymbol{\delta}$ is the identity tensor. Since the divergence of the Maxwell stress tensor is zero in the bulk of the fluid, (2.7) can be written as

$$-\nabla p_i + \mu_i \nabla^2 \boldsymbol{v}_i = 0. \tag{2.9}$$

Fluid velocities satisfy no-slip and no-penetration at the substrates

$$\boldsymbol{v}_1 = 0 \quad \text{at} \quad z = \beta H, \tag{2.10}$$

$$\boldsymbol{v}_2 = 0 \quad \text{at} \quad z = -H, \tag{2.11}$$

with appropriate continuity of velocity and stress conditions at the interface, $z = h(x, t)$

$$\|\boldsymbol{v}_i \cdot \boldsymbol{n}\| = 0, \tag{2.12}$$

$$\|\boldsymbol{v}_i \cdot \boldsymbol{t}\| = 0, \tag{2.13}$$

$$\|\boldsymbol{n} \cdot \boldsymbol{T}_i \cdot \boldsymbol{n}\| = \gamma \kappa, \tag{2.14}$$

$$\|\boldsymbol{n} \cdot \boldsymbol{T}_i \cdot \boldsymbol{t}\| = 0. \tag{2.15}$$

Here, $\kappa = [(\boldsymbol{\delta} - \boldsymbol{nn}) \cdot \nabla] \cdot \boldsymbol{n}$ is the interfacial curvature.

Additionally, one needs to specify evolution equations for the interfacial height and charge. These equations are provided through the kinematic boundary condition

$$\frac{\partial h}{\partial t} = v_z - v_x \frac{\partial h}{\partial x}, \tag{2.16}$$

and interfacial charge balance

$$\frac{\partial q}{\partial t} + v_x \frac{\partial q}{\partial x} = q\boldsymbol{n} \cdot (\boldsymbol{n} \cdot \nabla)\boldsymbol{v} + \|\sigma_i \boldsymbol{E}_i \cdot \boldsymbol{n}\|, \tag{2.17}$$

where all terms in both equations are evaluated at the interface $z = h(x, t)$.

2.2. Scalings

Dimensionless variables (all denoted by an overbar) are defined as follows:

$$\begin{aligned}
(z, h) &= H(\bar{z}, \bar{h}), & x &= L\bar{x}, & t &= T\bar{t}, \\
(\psi_i, V(t)) &= \chi(\bar{\psi}_i, \bar{V}(t)), & q &= Q\bar{q}, & p_i &= P\bar{p}_i, \\
v_z &= U\bar{v}_z, & v_x &= W\bar{v}_x.
\end{aligned} \tag{2.18}$$

In these equations, H is the thickness of the lower fluid layer and the time scale is defined by the vertical velocity component $T = H/U$. Balancing terms in the mass conservation equation (2.6) gives the horizontal velocity scale $W = UL/H$ in terms of the vertical velocity scale, while balancing terms in the interfacial charge condition (2.4) gives the charge scale $Q = \varepsilon_0 \chi / H$. The pressure scale is obtained through a balance between pressure and electrical stress in the normal stress balance (2.14), $P = \varepsilon_0 \chi^2 / H^2$. An inspection of the tangential component of the momentum balance equations (2.9) shows that a balance between the pressure and viscous stress terms in the lower fluid provides a vertical velocity scale $U = \varepsilon_0 \chi^2 H/(\mu_2 L^2)$. This leads to a horizontal length scale by balancing surface tension and electrical stresses in (2.14), $L = [\gamma H^3 / (\varepsilon_0 \chi^2)]^{1/2}$. In these scalings, the potential scale is determined by the maximum applied voltage $\chi = \max[V(t)]$.

Application of these scalings to the equations of § 2.1 generates eight dimensionless groups that are important for analysing this problem. The first six, the initial height ratio (layer 1/layer 2) β, viscosity ratio $\eta = \mu_1/\mu_2$, dielectric constants ε_i, and conductivities $S_i = L\sigma_i/(U\varepsilon_0)$, have been seen in previous studies. Additionally, for the dimensionless AC electrostatic potential at the bottom substrate, we define $V(t) = 1 + AC[\cos(\omega t) - 1]$. This provides two additional parameters. First is the relative AC magnitude, which ranges from $AC = 0$ for a pure DC potential to $AC = 1$ for a pure AC potential. Second is the dimensionless frequency , which is the product of the dimensional frequency with the process time scale $\omega = \Omega T$.

2.3. Evolution equations

To obtain nonlinear evolution equations for the interfacial height and charge, the equations of § 2.1 are first non-dimensionalized by the scalings of § 2.2. Consistent with the lubrication approximation, we consider the leading-order terms in an asymptotic expansion of the ratio of the vertical to horizontal length scales, H/L, in the limit $H/L \to 0$. The subsequent non-dimensional equations can then be manipulated into two evolution equations for the interfacial height and charge. This derivation is similar to that shown in previous works and will be omitted here for brevity; see S. A. Roberts (2009, in preparation) for the full derivation. The final nonlinear evolution equations are

$$\frac{\partial h}{\partial t} = -\frac{1}{2}(1+h)h'\left(2B_4 - (-1+h)\frac{\partial p_2}{\partial x}\right) - \frac{1}{6}(1+h)^2\left(3B_4' + (-2+h)\frac{\partial^2 p_2}{\partial x^2}\right) \tag{2.19}$$

$$\frac{\partial q}{\partial t} = S_1 B_1 - S_2 B_2 - qh'\left(B_4 + h\frac{\partial p_2}{\partial x}\right) - \frac{1}{2}(1+h)\left(2B_4 + (-1+h)\frac{\partial p_2}{\partial x}\right)q'$$

$$- \frac{1}{2}(1+h)\left(2B_4' + (-1+h)\frac{\partial^2 p_2}{\partial x^2}\right)q, \tag{2.20}$$

where the primes denote differentiation with respect to x. The expressions B_i and $\mathrm{d}p_i/\mathrm{d}x$ are complicated and were obtained by solving the underlying equations in *Mathematica*. Expressions for these constants are found in Appendix A.1.

2.4. Base state and normal mode expansion

We first consider the base state of the system, where the interface is flat and located at $z = 0$, $\boldsymbol{v}_i = 0$, and all variables are functions of z only. The electrostatic potential, governing equations and boundary conditions remain unchanged and can be solved

in terms of the base-state charge $\bar{q}(t)$

$$\bar{\psi}_1 = \frac{(\bar{q}(t) + \varepsilon_2 V(t))(\beta - z)}{\varepsilon_1 + \beta\varepsilon_2}, \quad \bar{\psi}_2 = \frac{(1 + z)\beta\bar{q}(t) + (\beta\varepsilon_2 - \varepsilon_1 z)V(t)}{\varepsilon_1 + \beta\varepsilon_2}, \quad (2.21)$$

where base-state quantities are denoted by an overbar.

These potentials can then be inserted into the charge evolution equation (2.17) and integrated in time with the initial condition $\bar{q}(0) = 0$, giving the expression

$$\bar{q}(t) = D_1 + D_2 \left[D_3 \exp(-D_6 t) + D_4 \sin(\omega t) - D_5 \cos(\omega t) \right], \quad (2.22)$$

where $D_1 = (AC - 1)(S_1\varepsilon_2 - S_2\varepsilon_1)/(S_1 + S_2\beta)$ and the remainder of the D_i are found in Appendix A.2. Of particular interest in understanding the interfacial stability of the system, as will be fully discussed in §4.1, is the maximum value of the base-state charge after a quasi-steady state has been reached ($t \to \infty$). Removing the asymptotic decay term of (2.22) ($D_3 \to 0$) and maximizing the remaining expression with respect to time yield the expression

$$\bar{q}_0 = \frac{(S_1\varepsilon_2 - S_2\varepsilon_1)((AC - 1)D - AC(S_1 + S_2\beta))}{D(S_1 + S_2\beta)}, \quad (2.23)$$

with $D = \sqrt{(S_1 + S_2\beta)^2 + \omega^2(\varepsilon_1 + \beta\varepsilon_2)^2}$.

Additionally, the normal stress boundary condition (2.14) can be manipulated to yield an expression for the pressure jump across the interface in the base state

$$\bar{p}_2 - \bar{p}_1 = \frac{\varepsilon_2(\beta\bar{q}(t) - \varepsilon_1 V(t))^2}{2(\varepsilon_1 + \beta\varepsilon_2)^2} - \frac{\varepsilon_1(\bar{q}(t) + \varepsilon_2 V(t))^2}{\varepsilon_1 + \beta\varepsilon_2)^2}. \quad (2.24)$$

Using these base-state results, a linear stability analysis is carried out by first applying a normal mode expansion to the interfacial height and charge,

$$h(x, t) = 0 + \tilde{h}(t)\exp(ikx), \quad q(x, t) = \bar{q}(t) + \tilde{q}(t)\exp(ikx). \quad (2.25)$$

Here, the variables $\tilde{h}$ and $\tilde{q}$ are perturbation variables which are small with respect to the base state. By applying these to (2.19)–(2.20), linearizing around the base-state values and dividing by $\exp(ikx)$, the linearized evolution equations are found to be of the form

$$\frac{\partial\tilde{h}}{\partial t} = C_1 \left(\tilde{h}(t) \left[-C_2 k^4 + k^2 \left(C_3\bar{q}(t)^2 + C_4\bar{q}(t)V(t) + C_5 V(t)^2 \right) \right] \right.$$
$$\left. + \tilde{q}(t)k^2 \left[-C_6\bar{q}(t) + C_7 V(t) \right] \right), \quad (2.26)$$

$$\frac{\partial\tilde{q}}{\partial t} = \tilde{h}(t) \left[C_1\bar{q}(t) + C_{13}V(t) - C_1 C_9 k^4\bar{q}(t) \right.$$
$$+ C_1 k^2 \left(C_{11}\bar{q}(t)V(t)^2 + C_{12}\bar{q}(t)^2 V(t) - C_8\bar{q}(t)^3 \right) \Big]$$
$$+ \tilde{q}(t) \left[-C_{14} + C_1 k^2 \left(C_{16}\bar{q}(t)V(t) - C_{15}\bar{q}(t)^2 \right) \right]. \quad (2.27)$$

In these equations, the constants C_i depend only on physical parameters (β, η, ε_i, S_i, AC, ω) and are found in Appendix A.3.

2.5. *Limiting cases*

Below, we discuss some of the relevant simplifications to the model of §2.1, and the implications of the simplifications to the equations of §2.3–2.4. These limits have been used for comparison with other published results.

2.5.1. *DC electric field*

A DC field is obtained in the limit $AC \to 0$. In this case, the frequency terms ω will naturally disappear, and the equations reduce to those of Craster & Matar (2005). Additionally, calculations have been performed using our nonlinear evolution equations and linear stability analysis, and the results for $AC \to 0$ approach those of Craster & Matar (2005).

2.5.2. *Air top layer*

A simpler case experimentally is when the top layer is air. This simplification involves taking three limits, $\eta \to 0$ due to the relatively low viscosity of air (compared to a polymer melt), $\varepsilon_1 \to 1$ and $S_1 \to 0$ as air is not conductive. When these simplifications are simultaneously applied with the limit $AC \to 0$, the equations and calculations match with those presented in previous works (Pease & Russel 2002; Craster & Matar 2005).

2.5.3. *Perfect dielectric layers*

Correctly deriving the equations for perfect dielectric fluids (where there is no conductivity in the bulk) is slightly less obvious than the previously described limits. At first glance, it may appear as simple as taking the limits $S_1, S_2 \to 0$. However, a careful inspection of the nonlinear charge evolution equation (2.17) reveals that the first two terms are not zero, allowing charge to exist at the interface. For this reason, the interfacial charge must also be set to zero, $q = 0$ (Shankar & Sharma 2004).

3. Perfect dielectric analysis

We begin our analysis by considering perfect dielectric fluids discussed in § 2.5.3. We first present a linear stability analysis and then show the results of nonlinear simulations.

3.1. *Linear stability analysis*

To perform the linear stability analysis for a perfect dielectric system, the evolution equations (2.26)–(2.27) are simplified by setting $q(t) = 0$. The system is then reduced to a single evolution equation

$$\frac{\partial h}{\partial t} = C_1 h(t)(-C_2 k^4 + k^2 C_5 V(t)^2). \tag{3.1}$$

As originally defined in § 2.2, $V(t) = 1 + AC\,[\cos(\omega t) - 1]$. Since this is a first-order ordinary differential equation (ODE), the equation is analytically integrated to obtain the expression

$$h(t) = E_1 \exp[(E_2 k^2 - E_3 k^4)t + E_4 k^2 \sin(\omega t) + E_5 k^2 \sin(2\omega t)]. \tag{3.2}$$

In this equation, E_1 represents the initial interface height, taken to be a small perturbation, $E_2 = (1/2)(2 - 4AC + 3AC^2)C_1C_5$ corresponds to the destabilizing force due to the electrostatic field, $E_3 = C_1C_2$ corresponds to the stabilizing surface tension force, and $E_4 = 2(AC - 1)AC\,C_1C_5/\omega$ and $E_5 = AC^2C_1C_5/(4\omega)$ arise from oscillatory terms due to the AC field. The expressions involving E_2 and E_3 represent an exponential growth, and $(E_2 k^2 - E_3 k^4)$ is the growth rate. It is also important to note that in the limit of DC fields $AC \to 0$, (3.2) reduces exactly to the growth rate expression in Shankar & Sharma (2004).

To better understand the behaviour that AC fields bring to the problem, it is instructive to initially study a simpler case that where the top layer is air ($\varepsilon_1 \to 1$,
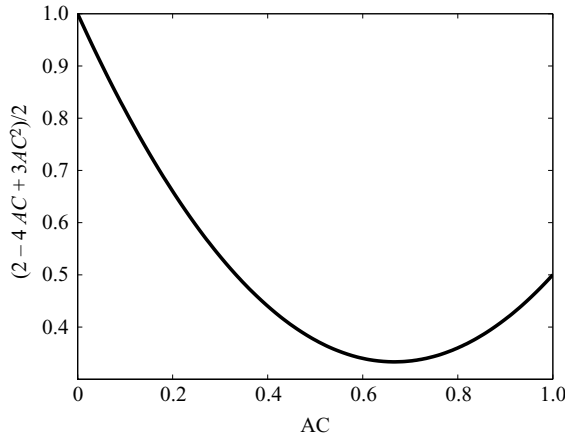
FIGURE 2. Behaviour of the additional AC term in the growth rate expression (3.3).

$\eta \to 0$) and the bottom layer is a perfect dielectric; the full case of two perfect dielectric liquids is discussed in the last paragraph of this section. In this simpler case the growth rate α is

$$\alpha = \frac{(2 - 4AC + 3AC^2)(\varepsilon_2 - 1)^2 \varepsilon_2}{6(1 + \beta \varepsilon_2)^3} k^2 - \frac{1}{3} k^4. \tag{3.3}$$

One unique feature of the AC field is the addition of the $(2 - 4AC + 3AC^2)/2$ term in the electrostatic destabilization term of the growth rate. This term arises through the integration of $V(t)^2$ and is the mean square potential. Examining the behaviour of this term, shown in figure 2, reveals that the destabilizing force of the electrostatic field, and therefore the growth rate, is maximized at $AC = 0$, a DC field, and goes through a minimum at $AC = 2/3$. Therefore, applying an AC field is equivalent to applying a DC field with magnitude equal to the mean square AC potential.

Similarly, the fastest-growing wavenumber, k_{max}, can be found by maximizing the growth rate. Thus,

$$k_{max} = \frac{1}{2} \sqrt{\frac{(2 - 4AC + 3AC^2)(\varepsilon_2 - 1)^2 \varepsilon_2}{(1 + \beta \varepsilon_2)^3}}, \tag{3.4}$$

$$\alpha_{max} = \frac{(2 - 4AC + 3AC^2)^2 (\varepsilon_2 - 1)^4 \varepsilon_2^2}{48(1 + \beta \varepsilon_2)^6}, \tag{3.5}$$

where α_{max} is the corresponding growth rate. The cutoff wavenumber, which is the largest unstable wavenumber, is $k_{cutoff} = \sqrt{2} k_{max}$. Again, the appearance of the mean square AC potential in all of these expressions causes the fastest-growing wavenumber and growth rate to be largest at $AC = 0$, with AC fields producing pillars that are slower growing and more widely spaced than those obtained by DC fields.

The remaining terms in (3.2) provide the oscillatory behaviour that is expected of an AC field. There are two components to this term; the $\sin(\omega t)$ term provides oscillations with the same frequency as the applied field, and the $\sin(2\omega t)$ term provides a response with twice the frequency. For a DC field, both of these terms are zero, as expected. In the pure AC limit, $AC = 1$, the $\sin(\omega t)$ term goes away, yielding a purely 2ω frequency response. This 2ω response is similar to that noted by Yih (1968) for a

pure AC field. At intermediate values of *AC*, the behaviour is a mixture of ω and 2ω frequencies.

Additionally, looking at the coefficients of these terms tells us about the amplitude of oscillation. Primarily, the coefficients of both terms scale as ω^{-1}, meaning that the amplitude of the interface oscillations should decrease with an increase in the frequency. This trend is reasonable because as the frequency increases, the interface has less time to flatten under a weak electric field before the electrostatic forces again pull the peaks towards the mask. This leads to less overall motion, or oscillation, in the pillars.

Growth rates may also be calculated for the original case of two perfect dielectric layers by inspecting the terms in (3.2). Even though the terms in this expression are slightly more complicated, the AC behaviour previously discussed in this section remains the same. For example, the fastest-growing wavenumber and growth rate for this case are

$$k_{max} = \frac{1}{2}\sqrt{\frac{(2 - 4AC + 3AC^2)(\varepsilon_2 - \varepsilon_1)^2\varepsilon_1\varepsilon_2}{(\varepsilon_1 + \beta\varepsilon_2)^3}}, \tag{3.6}$$

$$\alpha_{max} = \frac{(2 - 4AC + 3AC^2)^2(\varepsilon_2 - \varepsilon_1)^4\varepsilon_1^2\varepsilon_2^2\beta^3(\beta + \eta)}{48(\varepsilon_1 + \beta\varepsilon_2)^6\left(\beta^4 + 4\beta\eta + 6\beta^2\eta + 4\beta^3\eta + \eta^2\right)}, \tag{3.7}$$

and again the cutoff wavenumber is $k_{cutoff} = \sqrt{2}k_{max}$. These results are consistent with the previous studies of Shankar & Sharma (2004).

3.2. *Nonlinear simulations*

Nonlinear simulations were carried out to probe the behaviour that AC fields introduce outside the linear regime and to verify the linear stability results of § 3.1. Nonlinear evolution equations (2.19)–(2.20) are first simplified according to the perfect dielectric fluid assumptions (§ 2.5.3) to obtain a single evolution equation

$$\frac{\partial h}{\partial t} = -\frac{1}{2}(1 + h)h'\left(2F_1 - (-1 + h)F_2\right) - \frac{1}{6}(1 + h)^2\left(3F_1' + (-2 + h)F_2'\right), \tag{3.8}$$

with

$$F_1 = F_3(\beta - h)^2(-2(1 + \beta)\eta + h(\beta^2 - \eta + (-1 + \eta)(2\beta - h)h)),$$
$$F_2 = -F_3(\beta - h)^2(\beta^2 + 3\eta + 4\beta\eta + h(-2\beta + 2\eta + 4\beta\eta + h - \eta h)),$$
$$F_3 = (\varepsilon_1(\varepsilon_1 - \varepsilon_2)^2\varepsilon_2 V(t)^2 h' + (\varepsilon_1 + \beta\varepsilon_2 + (\varepsilon_1 - \varepsilon_2)h)^3 h''')$$
$$/((\varepsilon_1 + \beta\varepsilon_2 + (\varepsilon_1 - \varepsilon_2)h)^3(\beta^4 + 2\beta(2 + \beta(3 + 2\beta))\eta + \eta^2 + (-1 + \eta)h$$
$$(4(\beta^3 + \eta) + h(-6\beta^2 + 6\eta + 4(\beta + \eta)h + (-1 + \eta)h^2)))),$$

where $h = h(x, t)$ and $V(t) = 1 + AC\left[\cos(\omega t) - 1\right]$.

This evolution equation is discretized over the solution domain using fourth-order accurate finite-difference formulae on an evenly spaced grid. Periodic boundary conditions are implemented at the horizontal boundaries. A van der Waals-like repulsive force is imposed at the mask and substrate to prevent the liquid interface from penetrating the surfaces, causing film breakup. The form of this repulsive force is similar to that in equation (3) of Wu *et al.* (2005). For clarity, these force terms have not been included in the equations presented here; the complete equations can be found in S.A. Roberts (2009, in preparation). Time integration is implemented using DASPK3.0 (Brenan 1996), which uses fifth-order backward differentiation formulae with automatically adjusting time steps. For a typical simulation, the domain was taken to be six times the fastest-growing wavelength predicted by the linear stability
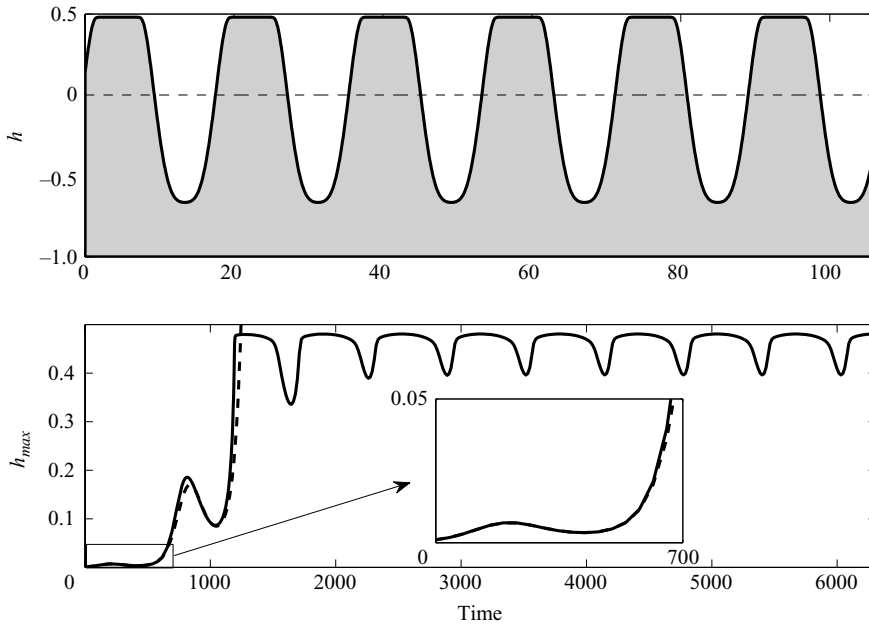
FIGURE 3. Sample simulation for a perfect dielectric system with $\beta = 0.5$, $\eta = 0$, $\varepsilon_1 = 1$, $\varepsilon_2 = 2.5$, $AC = 1$ and $\omega = 0.005$. The top panel shows the final interfacial profile. The bottom panel shows the evolution of the top of the pillars (h_{max}) through the evolution process, where the solid line is the nonlinear simulation result and the dashed line is that predicted by the linear stability analysis from (3.2).

analysis, and between 1000 and 2000 grid points were used. Initial conditions were typically given as a sinusoidal function with a wavelength matching that of the fastest-growing wavelength and with an amplitude of $\beta/1000$. These conditions enabled the fastest simulation times while maintaining solution accuracy, and were used for a majority of the simulations. However, a representative subset of these results was verified using random initial conditions and varying domain sizes.

Generally, nonlinear simulations yield results in qualitative agreement with linear stability predictions. Figure 3 shows a sample result from these simulations; there are a few key features to note. First, the initial growth matches nearly perfectly with the predictions of the linear stability analysis (3.2), including the time required for the interface to reach the top of the domain (t_{top}). Throughout the parameter space, these simulations consistently showed good agreement with the predicted growth rate (3.3) within the linear regime, where $h \ll \beta$. Second, the top panel shows exactly six pillars in the domain, corresponding to the domain size set by six times the fastest-growing wavelength from linear stability analysis. This result is typical and shows that linear stability analysis accurately predicts the pillar spacing in the nonlinear regime. Third, the time scale of the oscillatory response in the bottom panel is exactly twice the time scale of the electrostatic field, corresponding to the 2ω response predicted by the linear stability analysis for $AC = 1$.

After the initial growth phase, there is a transient period where the distance the pillar tops fall with each AC period decreases, as seen in the first few troughs in the bottom panel of figure 3. A quasi-steady-state period begins once these transients have subsided. If we define the overall pillar height as the difference between the pillar peak and trough, then we can define the quasi-steady-state height oscillation (QSSHO) as
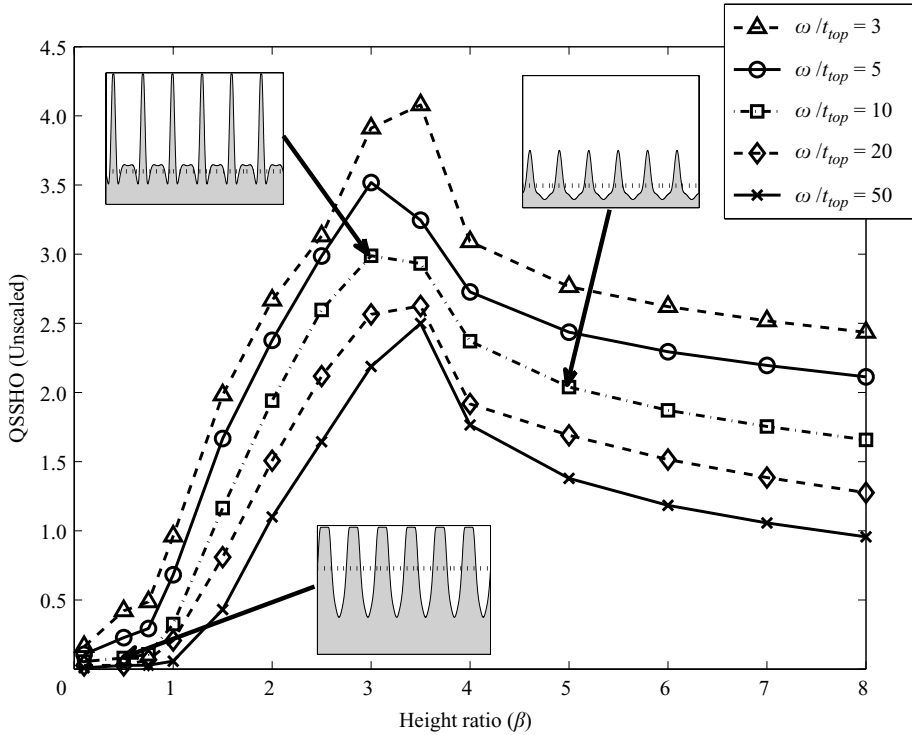
FIGURE 4. QSSHO vs. the height ratio (β) for a perfect dielectric with $\varepsilon_1 = 1$, $\varepsilon_2 = 2.5$, $\eta = 0$ and $AC = 1$. Inset figures depict representative interfacial profiles for three points.

the difference between the maximum and minimum overall pillar heights once the quasi-steady-state period has been reached. General trends for the QSSHO are shown in figure 4; each curve in this figure is for a given value of ω/t_{top}. This quantity t_{top} has been found to be an important time scale for correlating simulation results. The first key result from this plot is that the overall QSSHO decreases as ω/t_{top} decreases. This result is logical, since with a lower frequency, the pillars experience a longer time each period with a weak electric field. Therefore, the pillars have more time to relax towards the base state in each period of the AC cycle. This yields larger amplitude oscillations. Secondly, there are three distinct zones of height ratio variance in this plot. At low height ratios, $\beta < 2.5$, the QSSHO increases with the height ratio. In this regime, the pillars consistently reach the top mask and increasing β gives the pillars more room to oscillate. Near $\beta = 3$, there is a peak in the QSSHO, corresponding to the point where the pillars are just reaching the top mask. Beyond $\beta = 3$, there is a sharp decrease which levels out to a nearly constant value. In this region, pillars do not reach the top mask and their heights remain relatively constant with the height ratio, leading to the QSSHO behaving similarly. In general, the pillar shape under AC fields is similar to that under DC fields, except for a thinning of the pillars, a phenomenon that is discussed in more detail in § 4.2.

While AC fields may not be used to directly make smaller diameter pillars than the corresponding DC field, they do allow a degree of control over the overall spacing of the pillars. The QSSHO may also be controlled by adjusting the frequency of the AC field, with higher frequencies leading to smaller oscillations in the pillar heights.

This behaviour may be important in dynamic applications, where one desires precise control of periodic changes in the interface topography.

4. Leaky dielectric analysis

Now that the basic interactions of AC electric fields with perfect dielectric fluids have been explored, we move on to the more complicated and more physically appropriate leaky dielectric model. We begin with a stability analysis using Floquet theory, then present the results of nonlinear simulations.

4.1. *Floquet analysis*

For the leaky dielectric model, the full linearized equations (2.26)–(2.27) must be solved for the growth rate. Perfect dielectrics yield a single first-order ODE with a non-constant coefficient, which can be solved analytically. Leaky dielectrics, however, yield two coupled first-order ODEs with non-constant coefficients which cannot be integrated analytically; instead, the techniques of Floquet theory must be utilized.

First, we assume that the perturbation quantities can be represented by the Floquet expansions

$$\tilde{h}(t) = \sum_n \hat{h}_n \exp\left[(\alpha + \mathrm{i}(n+\gamma)\omega)\,t\right], \quad \tilde{q}(t) = \sum_n \hat{q}_n \exp\left[(\alpha + \mathrm{i}(n+\gamma)\omega)\,t\right], \quad (4.1)$$

where n is the integer-frequency multiplier γ is the Floquet harmonic parameter (where $0 \leqslant \gamma \leqslant 1/2$; $\gamma = 0$ corresponds to a harmonic response and $\gamma = 1/2$ is a subharmonic response), ω is the frequency of the AC field and α is the real-valued growth rate, as previously discussed. If we perform this Floquet expansion and substitute in the expressions for $\bar{q}(x,t)$ and $V(t)$, we can divide by $\exp(\alpha t)$ and collect terms in the same power of $\exp(\mathrm{i}n\omega t)$ to obtain

$$\hat{h}_n \big[(G_1^0 - \alpha - \mathrm{i}(n+\gamma)\omega)\mathrm{e}^{\mathrm{i}(n+\gamma)\omega t} + G_1^1 \mathrm{e}^{\mathrm{i}(n+\gamma+1)\omega t} + G_1^{1\dagger}\mathrm{e}^{\mathrm{i}(n+\gamma-1)\omega t}$$
$$+ G_1^2 \mathrm{e}^{\mathrm{i}(n+\gamma+2)\omega t} + G_1^{2\dagger}\mathrm{e}^{\mathrm{i}(n+\gamma-2)\omega t} + G_1^3 \mathrm{e}^{\mathrm{i}(n+\gamma+3)\omega t} + G_1^{3\dagger}\mathrm{e}^{\mathrm{i}(n+\gamma-3)\omega t}\big]$$
$$\hat{q}_n \big[G_2^0 \mathrm{e}^{\mathrm{i}(n+\gamma)\omega t} + G_2^1 \mathrm{e}^{\mathrm{i}(n+\gamma+1)\omega t} + G_2^{1\dagger}\mathrm{e}^{\mathrm{i}(n+\gamma-1)\omega t}$$
$$+ G_2^2 \mathrm{e}^{\mathrm{i}(n+\gamma+2)\omega t} + G_2^{2\dagger}\mathrm{e}^{\mathrm{i}(n+\gamma-2)\omega t} + G_2^3 \mathrm{e}^{\mathrm{i}(n+\gamma+3)\omega t} + G_2^{3\dagger}\mathrm{e}^{\mathrm{i}(n+\gamma-3)\omega t}\big] = 0, \quad (4.2)$$

$$\hat{h}_n \big[G_3^0 \mathrm{e}^{\mathrm{i}(n+\gamma)\omega t} + G_3^1 \mathrm{e}^{\mathrm{i}(n+\gamma+1)\omega t} + G_3^{1\dagger}\mathrm{e}^{\mathrm{i}(n+\gamma-1)\omega t}$$
$$+ G_3^2 \mathrm{e}^{\mathrm{i}(n+\gamma+2)\omega t} + G_3^{2\dagger}\mathrm{e}^{\mathrm{i}(n+\gamma-2)\omega t} + G_3^3 \mathrm{e}^{\mathrm{i}(n+\gamma+3)\omega t} + G_3^{3\dagger}\mathrm{e}^{\mathrm{i}(n+\gamma-3)\omega t}\big]$$
$$\hat{q}_n \big[(G_4^0 - \alpha - \mathrm{i}(n+\gamma)\omega)\mathrm{e}^{\mathrm{i}(n+\gamma)\omega t} + G_4^1 \mathrm{e}^{\mathrm{i}(n+\gamma+1)\omega t} + G_4^{1\dagger}\mathrm{e}^{\mathrm{i}(n+\gamma-1)\omega t}$$
$$+ G_4^2 \mathrm{e}^{\mathrm{i}(n+\gamma+2)\omega t} + G_4^{2\dagger}\mathrm{e}^{\mathrm{i}(n+\gamma-2)\omega t} + G_4^3 \mathrm{e}^{\mathrm{i}(n+\gamma+3)\omega t} + G_4^{3\dagger}\mathrm{e}^{\mathrm{i}(n+\gamma-3)\omega t}\big] = 0, \quad (4.3)$$

where the G_i^j are found in Appendix A.4 and $\dagger$ represents the complex conjugate. If we now let $-N \leqslant n \leqslant N$ and truncate all terms $\exp(\mathrm{i}m\omega t)$ where $|m| > N$, then we can form a $4N+2$ by $4N+2$ eigensystem $\boldsymbol{A}\boldsymbol{x} = \lambda\boldsymbol{x}$, where the $4N+2$ eigenvalues are $\lambda = \alpha + \mathrm{i}(n+\gamma)\omega$ and the eigenvectors are $\hat{h}_n$ and $\hat{q}_n$, which are each associated with a corresponding power of $\exp(\mathrm{i}m\omega t)$. This eigensystem is solved using the standard eigensystem solution capabilities of MATLAB. In these calculations, N was increased until sufficient resolution was achieved. The Floquet parameter γ was always found to be zero. The largest real eigenvalue is chosen as the growth rate, using a method similar to that of González *et al.* (2003).
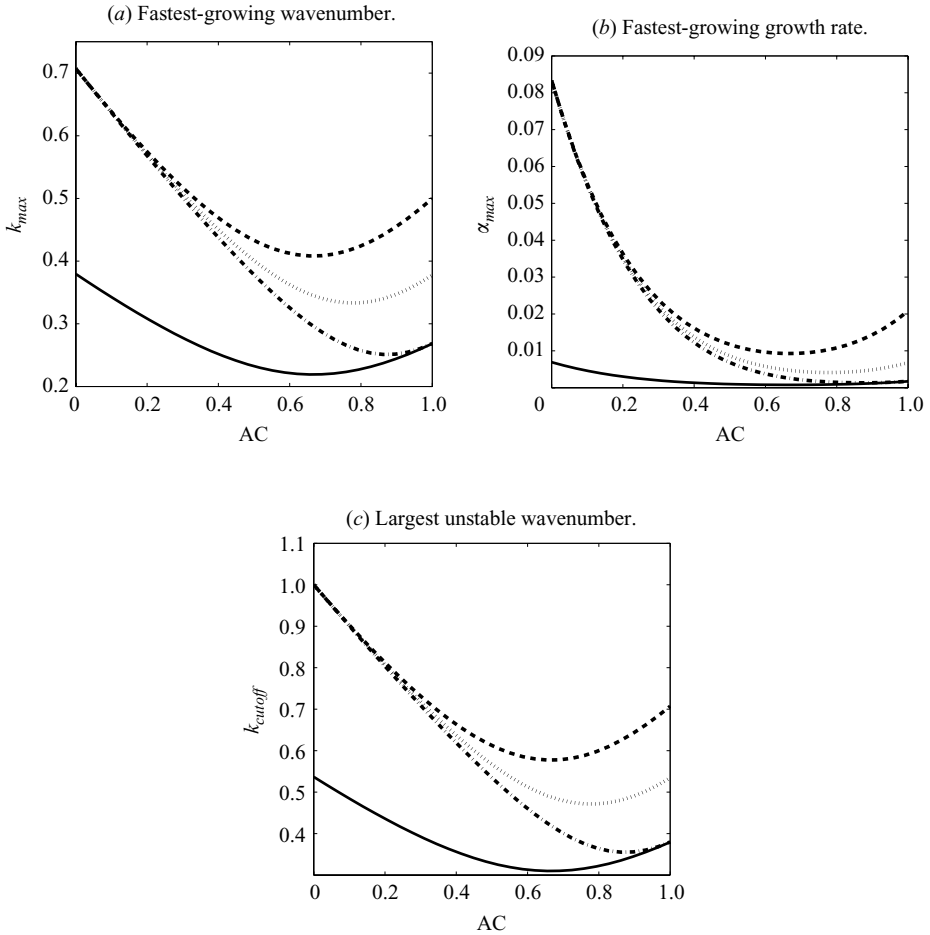
(*a*) Fastest-growing wavenumber.

(*b*) Fastest-growing growth rate.

(*c*) Largest unstable wavenumber.

FIGURE 5. Effect of the AC parameter on the growth rates and wavenumbers for leaky and perfect dielectrics under various frequencies; $(- - -)$ $\omega = 10^1$, $(\cdots)$ $\omega = 10^{2.5}$, $(- \cdot -)$ $\omega = 10^4$ and $(—)$ perfect dielectric. All plots are for $\beta = 1$, $\eta = 0$, $\varepsilon_1 = 1$, $\varepsilon_2 = 4$, $S_1 = 0$ and $S_2 = 10^3$.

Allowing even minuscule amounts of charge accumulation at the interface ($S_i > 0$) yields a drastic increase in the fastest-growing growth rates and a marked increase in the fastest-growing wavenumber, a fact noted by Pease & Russel (2002). This charge will tend to accumulate at the top of the pillars, causing the the electric field to have a greater effect on the pillar tips, effectively pulling them towards the mask with greater speed than would happen with a uniform charge distribution. AC fields, however, generally have a similar effect in leaky dielectrics as they do in perfect dielectrics, namely that the growth rates and wavenumbers are lower in the AC case than in the DC case. Specific examples of this behaviour are illustrated in figure 5. In the limit of a DC field ($AC = 0$), there are two possible values for the growth rate or wavenumber, those for a perfect dielectric or a leaky dielectric, as the frequency has no influence in DC fields. As the AC parameter is increased at low frequencies, the leaky dielectric results behave similar to those of the perfect dielectric, with wavenumbers and growth rates first decreasing, then increasing past $AC = 2/3$. However, increasing the frequency in situations with a high value of AC leads to suppression of interfacial charge, as discussed in the next paragraph, with the growth rate and wavenumber
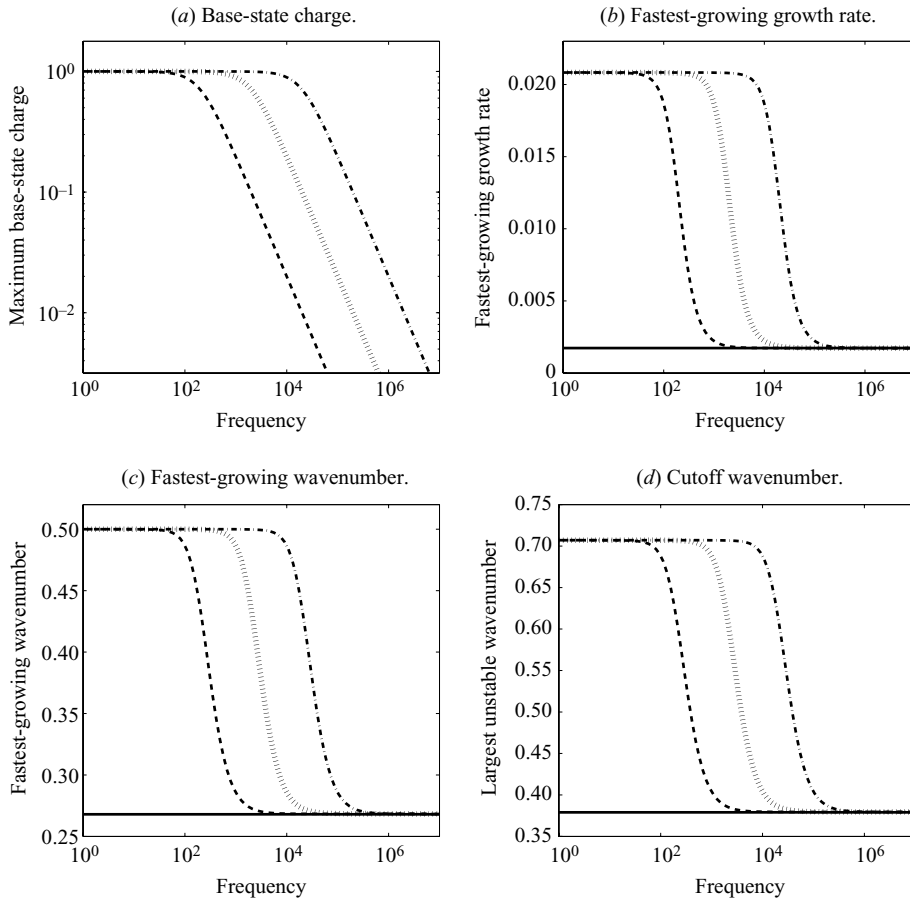
FIGURE 6. Effect of frequency on base-state charge and Floquet results for varying lower layer conductivity; $(- - -)$ $S_2 = 10^3$, $(\cdots)$ $S_2 = 10^4$, $(- \cdot -)$ $S_2 = 10^5$ and (---) perfect dielectric $S_2 = 0$. All plots are for $\beta = 1$, $\eta = 0$, $AC = 1$, $\varepsilon_1 = 1$, $\varepsilon_2 = 4$ and $S_1 = 0$.

values eventually reaching those of the perfect dielectric fluid at $AC = 1$ and high frequencies.

The most significant impact that AC fields have is the effect of the AC field frequency on the base-state charge, as highlighted in figure 6. A careful inspection of (2.23) shows that there are two distinct regimes of behaviour; one where $S_1 + S_2 \gg \omega$ and one where $S_1 + S_2 \ll \omega$. In the first case, where the dimensionless conductivity is much larger than the forcing frequency, the base-state charge is independent of frequency, a behaviour shown in the low-frequency region of figure 6(*a*). As the frequency increases, however, the relatively low conductivity of the fluid inhibits the movement of charge within the medium, as the oscillation time scale ($1/\omega$) is much less than the time scale for charge transport ($1/S_2$), effectively making the fluid a perfect dielectric. In this range of high frequency, the maximum base-state charge scales as ω^{-1}, also shown in figure 6(*a*).

The impact of this base-state charge behaviour can be easily seen in the critical wavenumbers and growth rates shown in figure 6(*b–d*). As the frequency approaches the value of the conductivity, the critical values begin to drop drastically. These values eventually saturate exactly at their perfect dielectric values as the frequency continues
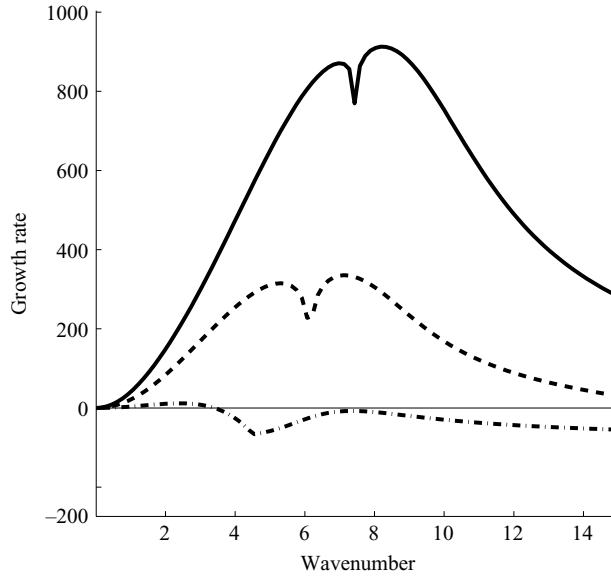
FIGURE 7. Growth rate curves showing dual-hump behaviour for varying frequency; (——) $\omega = 1 \times 10^2$, (— — —) $\omega = 1.5 \times 10^2$ and (— · —) $\omega = 5 \times 10^2$. Here, $AC = 1$, $\beta = 0.1$, $\eta = 0$, $\varepsilon_1 = 1$, $\varepsilon_2 = 4$, $S_1 = 0$ and $S_2 = 10^3$.

to increase. These results support the previous statement that if the frequency is greater than the conductivity, the charges cannot move to the interface quickly enough, and therefore the leaky dielectric fluid now acts as a perfect dielectric. Although figure 6 shows results for the case where the bottom layer has a larger dielectric constant and conductivity, the same generic behaviour is observed if either one or both of these quantities is smaller in the bottom layer. We emphasize that the details of the transition from leaky dielectric behaviour to perfect dielectric behaviour shown in figure 6 could not have been determined without carrying out a careful Floquet analysis as we have done. Unlike the perfect dielectric case considered in §3, all of the temporal modes in the linear stability analysis couple to one another in leaky dielectric fluids when AC fields are present.

At low height ratios ($\beta \lesssim 0.1$), we have noticed a particularly interesting behaviour, the appearance of dual peaks, or local maxima, in the growth rate curve. This behaviour, as illustrated in figure 7, is seen exclusively in leaky dielectric materials under AC fields and only at low height ratios ($\beta \lesssim 0.1$). At higher frequencies the higher-wavenumber peak is completely stable ($\alpha < 0$), and only a single peak is unstable. For typical parameter values, when there is only one peak in the growth rate curve, the fastest-growing wavenumber is easy to identify. However, when there are similarly sized peaks at two wavenumbers, one might expect a competition in growth between the two peaks, and it is not necessarily clear which wavenumber dominates. In §4.2, we discuss the results of nonlinear simulations to verify the wavenumber that ultimately grows and survives.

The results of this section are significant, as they provide two mechanisms to exert further control over the wavenumbers, and therefore pillar spacings, that are achievable using EHD instabilities; the relative AC field contribution and the frequency of that field. Using the example shown in figure 5, only two wavenumbers are achievable with a DC field, those for a leaky dielectric and a perfect dielectric.
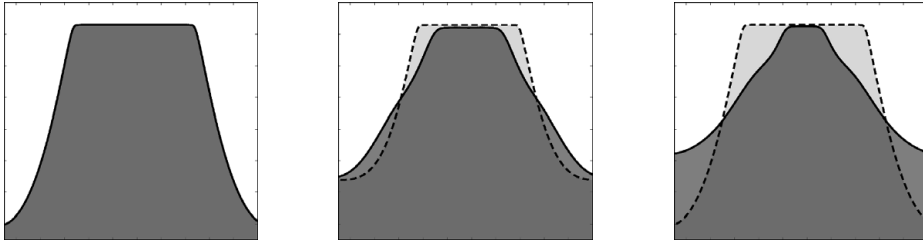
FIGURE 8. Evolution of a single pillar profile for a DC field (light grey) and after the AC field is applied (dark grey). Constants are $\omega = 10^5$, $\beta = 0.25$, $\eta = 0$, $\varepsilon_1 = 1$, $\varepsilon_2 = 4$, $S_1 = 0$ and $S_2 = 10^8$.

However, by manipulating the AC parameter and frequency, one can achieve a range of wavenumbers without changing physical parameters such as the height ratio, viscosity ratio or overall field strength. While it is known that AC fields suppress charge accumulation (Devitt & Melcher 1965; Reynolds 1965), the effect of that suppression on the fastest-growing wavenumbers was previously unknown.

4.2. *Nonlinear simulations*

Nonlinear evolution equations (2.19)–(2.20) were solved using the same finite-difference scheme presented in §3.2. The nonlinear simulations agreed with the predictions of the Floquet analysis in terms of growth rates, wavenumbers and frequency response. For brevity, numerical comparisons will not be shown here, as the results are similar to those of figure 3. We will, however, discuss simulation results investigating the low-height-ratio behaviour of figure 7, along with noting two interesting features discovered during the course of the simulations which highlight the additional control mechanisms introduced by AC fields.

As discussed in §4.1 and illustrated in figure 7, Floquet theory predicts a competition between two wavenumbers to be the fastest-growing at very low height ratios. Nonlinear simulations in these situations verify this behaviour; the dominant wavelength seen during the initial growth phase is between the two wavenumbers corresponding to the two peaks from figure 7. Setting the horizontal simulation domain to be consistent with either one wavenumber or the other still yields pillars with wavenumbers between the two predicted wavenumbers. As soon as the frequency is increased enough for linear theory to predict the second hump falling below $\alpha = 0$ (figure 7, the bottom curve), the simulation results revert to those consistent with the one hump remaining unstable, verifying all aspects of this behaviour predicted by the linear theory.

As a primary motivation of this work is gaining a better understanding of how to control the size and shape of the pillars, we found that AC fields provide an additional level of control over the width of the pillars, a feature illustrated in figure 8. Under DC fields, patterns grow at a certain wavelength and reach a steady-state configuration with a certain pillar width, maximum pillar height and spacing between pillars. If, after the pillars have reached this steady state, the DC field is turned into an AC field (the AC parameter switched from zero to unity; a wide range of frequencies may be used), the interface will begin to oscillate and the pillar peaks will begin to thin. This phenomenon is due to the transient nature of the AC field. As the effective voltage decreases during each AC period, so does the force on the interface, allowing the tip of the pillar to thin and then drop away from the mask. When the frequency of the field is high enough, the pillar appears trapped in a thinner state, as the period of the
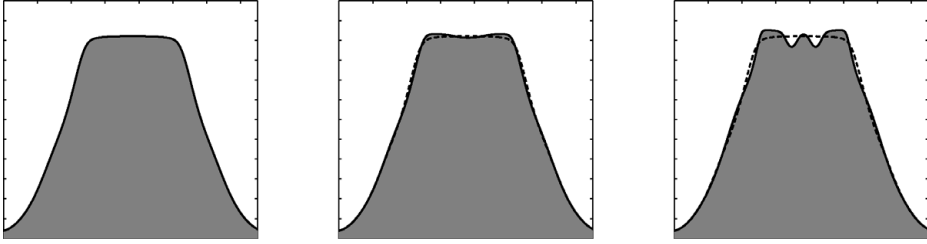
FIGURE 9. Evolution of pillar peak splitting for a system with $AC = 1$, $\omega = 10^5$, $\beta = 0.25$, $\eta = 0$, $\varepsilon_1 = 1$, $\varepsilon_2 = 4$, $S_1 = 0$ and $S_2 = 10^8$. The original peak in the first panel is shown as a dashed line in subsequent panels.

AC field is much shorter than the time required for the pillar to spread out at the maximum pillar height. Larger frequencies favour smaller height oscillations, similar to the behaviour shown in figure 4.

In the case of figure 8, the final AC pillar diameter is approximately one-third that of the DC case; this is further discussed in §5 and quantified in figure 10(a). For all parameter values observed (in both perfect and leaky dielectric systems), the ratio of the pillar diameter to the pillar spacing (fastest-growing wavelength) decreases when a DC field is switched to AC after the initial growth is complete. What is interesting about using a DC field for growth before switching to an AC field is that growing with the DC field locks in the pillar spacing at a smaller wavelength than is achievable using a comparable AC field, but the AC field can still subsequently thin the pillars, decreasing the width-to-spacing ratio. It is worth noting that the same phenomenon, however, does not occur when switching an AC field to a DC field, as this is a purely transient effect of the AC field.

Finally, a phenomenon we have come to call "peak splitting" has been observed for certain parameter values in leaky dielectric systems, and is illustrated in figure 9. At the top of the original peak, we see the formation of three subpeaks. While these peaks are dynamic features and do not stretch as deeply as the primary pillars do, they do show that it is possible to obtain feature sizes that are smaller than the typical DC pillars. This phenomenon generally occurs at low height ratios. Since a repulsive force is present between the fluid and the mask, the pillar tops reach an equilibrium distance away from the mask if a DC field is used. When AC fields are applied, the oscillation of the interface causes the average pillar height to be lower than that for a DC field. The space that appears above the pillars may be able to induce another instability on shorter time and length scales, which is manifested as these split peaks. This behaviour is purely a transient phenomenon and would not be seen under DC fields. We have used the Floquet analysis of the previous section to show qualitative, order-of-magnitude agreement with this hypothesis. Using figure 9 as an example, the small peaks shown in the third panel correspond to a wavelength of 0.55, while a linear stability analysis using the top of the flat peak as the initial height gives a predicted wavelength of 0.48.

5. Time-varying DC fields

While the previous sections of the paper were dedicated to the effects that time-periodic AC electric fields have on the control of EHD pillar formation, novel effects are also seen with non-periodic variation of the electric field. These time-varying DC
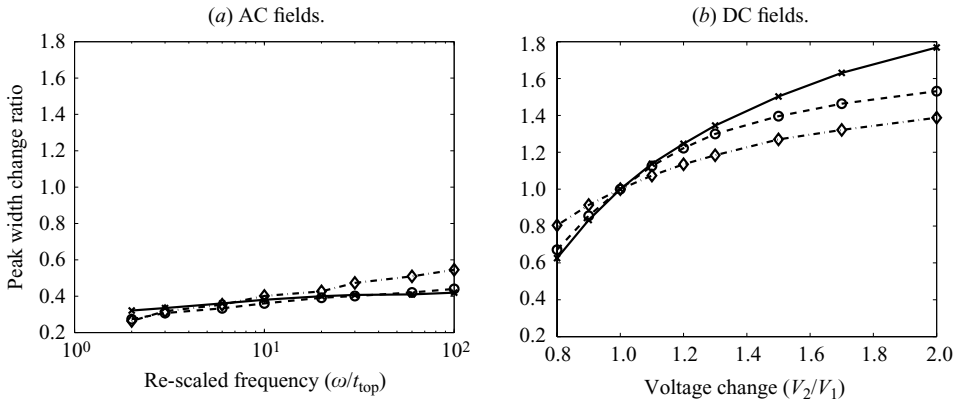
FIGURE 10. Thinning and thickening of pillars formed by initially using a DC field then switching to (*a*) an AC field or (*b*) a DC field of different amplitude after the pillar structure has formed. The *y*-axis is the ratio of the width of the pillars under the original DC field to the width after the field has changed. The width of each pillar is measured at five percent of the total pillar height below the top of the pillar. In the *x*-axis, V_1 is the original voltage used during the growth and for calculation of t_{top}, while V_2 is the voltage after the change is made. For (*a*), the minimum pillar width ratio (thinnest pillar) is reported. Data are plotted for various height ratios; (——×——) $\beta = 0.3$, (- - -○- - -) $\beta = 0.5$ and (- . -◇- . -) $\beta = 1$. Calculations are for a perfect dielectric bottom layer with $\varepsilon_2 = 4$ and an air top layer.

fields have not been explored in prior works, so we report some of our observations here.

The thinning of pillar peaks by switching to an AC field after pillar formation was discussed in §4.2 and illustrated in figure 8. Figure 10(*a*) shows that the amount of thinning which can be achieved through this switch has a slight frequency dependence. However, the overall range of thinning is limited to approximately one-third of the original pillar width. However, if instead of switching to an AC field after the pillars have formed, the DC voltage is simply changed to a different value, a similar effect is seen. When the voltage is decreased the pillar tip thins, and when the voltage is increased the tip thickens, a result shown in figure 10(*b*). The more the voltage deviates from the original voltage and the lower the height ratio, the stronger the thinning or thickening effect is. However, if the voltage is decreased below approximately 70 % of the original voltage, the pillars decay back to a flat interface rather than thinning. Thus, time-varying DC fields can be used to thin or thicken pillars, whereas switching from a DC field to an AC field can only thin pillars. However, the latter strategy produces more thinning than the former strategy as can be seen by comparing figures 10(*a*) and 10(*b*).

The above discussion applies to situations where the voltage switch (from DC to AC or another DC value) occurs after the pillars have fully formed. However, if this switch occurs before the pillars fully form, differences may appear. When the switch occurs late in the growth process, and the pillars are at least 50 % of their final height, no change is seen; the dynamics are the same as if the switch occurred later, forming pillars with a spacing consistent with the original voltage. However, if the switch occurs even earlier in the growth process, the pillars decay down to a flat interface and then later re-grow, but this time with a spacing consistent with the linear stability analysis predictions based solely on the final voltage.

Additionally, instead of making a step change to the voltage, a linear ramp from the initial voltage to the final voltage can be applied. This can also be done with a

ramp from a DC to an AC field. In these instances, the observed behaviour is highly dependent on the speed at which the ramp occurs. For relatively fast ramps, where the ramp length is similar to t_{top} for the original voltage, the behaviour is similar to the case where a step switch had been made late in the growth. However, if the time over which the ramp occurs lengthens, the observed behaviour is more complex, with pillar spacings between those predicted by the linear stability analysis for each of the two voltages. In all cases of ramps, the growth occurs much more slowly than if only a single voltage had been used.

6. Conclusions

We have presented a theoretical study of how AC electric fields may be used to control the formation of pillar-like structures in thin liquid films. Linear stability analysis for the case of perfect dielectric fluids shows that the influence of an AC field can be understood by considering an effective DC field. The use of an AC field shifts the EHD instability to longer wavelengths and slows its growth. Nonlinear simulations yield results consistent with the linear stability analysis, and reveal that the film height settles into a quasi-steady state where the film height oscillates with a frequency which, in general, is a mixture of the imposed oscillation frequency and its first harmonic. For leaky dielectric fluids, Floquet theory must be applied to obtain linear stability results. It is found that the frequency of the electric field has a strong effect on the accumulation of interfacial charge, and this in turn can be used to further tune the instability growth rate and wavenumber. In addition to confirming the linear stability results, the nonlinear simulations demonstrate how thinner pillars can be created by switching on an AC field after a DC field is applied. The creation of smaller-scale structures on top of the original peaks (peak splitting) is also observed for some parameter values, and is likely the result of a local instability. Additional dynamic phenomena were observed for various cases of time-varying DC fields, resulting in dramatic thinning or thickening of pillar widths.

As noted in the introduction, there are a number of practical applications where fine control over surface topography is required. While this need has motivated a number of studies involving DC fields, the present study suggests that AC fields may be fruitfully applied to further tailor topographical features. An important next step in this line of inquiry will be to extend the approach used here to two dimensions in order to explore how the oscillation amplitude and frequency influence the structure and symmetry of topographical patterns. Related work on the Faraday instability is expected to provide guidance in that endeavour, and the results may contribute both fundamental and practical insight into pattern formation in spatially extended dynamical systems.

Appendix. Equation details
A.1. *Nonlinear evolution equation details*
Here, we present expressions for the constants found in (2.19)–(2.20):

$$B_1 = -\frac{(1+h)q + \varepsilon_2 V(t)}{\varepsilon_1 + \beta\varepsilon_2 + (\varepsilon_1 - \varepsilon_2)h},$$

$$B_2 = \frac{(\beta - h)q - \varepsilon_1 V(t)}{\varepsilon_1 + \beta\varepsilon_2 + (\varepsilon_1 - \varepsilon_2)h},$$

$$\begin{aligned}
B_3 = &((1+h)(-(\beta - h)(3\beta^2 + 4\beta^3 + \eta - 3(\beta^2 - \eta)h + 3(-1+\eta)h^2 \\
&+(-1+\eta)h^3)q B_1' - B_1(\varepsilon_1(1+h)(2\beta^2(1+\beta) + (-\beta^2 + \eta)h + 2(-1+\eta)h^2 \\
&+(-1+\eta)h^3)B_1' - (3\beta^2 + 4\beta^3 + \eta - 3(\beta^2 - \eta)h + 3(-1+\eta)h^2 \\
&+(-1+\eta)h^3)qh') + (1+h)(2\beta^2(1+\beta) + (-\beta^2 + \eta)h + 2(-1+\eta)h^2 \\
&+(-1+\eta)h^3)(\varepsilon_2 B_2 B_2' - h'''))) / (\beta^4 + 4\beta\eta + 6\beta^2\eta + 4\beta^3\eta + \eta^2 \\
&+4(-1+\eta)(\beta^3 + \eta)h - 6(\beta^2 - \eta)(-1+\eta)h^2 \\
&+4(-1+\eta)(\beta + \eta)h^3 + (-1+\eta)^2 h^4),
\end{aligned}$$

$$\begin{aligned}
B_4 = &((\beta - h)((\beta - h)(\beta^3 + 4\eta + 3\beta\eta - 3(\beta^2 - \eta)h - 3\beta(-1+\eta)h^2 + (-1+\eta)h^3)q B_1' \\
&+ B_1(\varepsilon_1(\beta - h)(-2(1+\beta)\eta + (\beta^2 - \eta)h + 2\beta(-1+\eta)h^2 - (-1+\eta)h^3)B_1' \\
&- (\beta^3 + 4\eta + 3\beta\eta - 3(\beta^2 - \eta)h - 3\beta(-1+\eta)h^2 + (-1+\eta)h^3)qh') \\
&- (\beta - h)(-2(1+\beta)\eta + (\beta^2 - \eta)h + 2\beta(-1+\eta)h^2 - (-1+\eta)h^3)(\varepsilon_2 B_2 B_2' - h'''))) \\
&/ (\beta^4 + 4\beta\eta + 6\beta^2\eta + 4\beta^3\eta + \eta^2 + 4(-1+\eta)(\beta^3 + \eta)h - 6(\beta^2 - \eta)(-1+\eta)h^2 \\
&+4(-1+\eta)(\beta + \eta)h^3 + (-1+\eta)^2 h^4),
\end{aligned}$$

$$\begin{aligned}
\frac{\mathrm{d}p_1}{\mathrm{d}x} = &(\eta(1+h)(6(1+\beta)(\beta - h)^2 q B_1' + B_1(\varepsilon_1(1+h)(4\beta + 3\beta^2 + \eta - 2(2+\beta-\eta)h \\
&+(-1+\eta)h^2)B_1' - 6(1+\beta)(\beta - h)qh') - (1+h)(4\beta + 3\beta^2 \\
&+\eta - 2(2+\beta-\eta)h + (-1+\eta)h^2)(\varepsilon_2 B_2 B_2' - h'''))) / (\beta^4 + 4\beta\eta + 6\beta^2\eta \\
&+4\beta^3\eta + \eta^2 + 4(-1+\eta)(\beta^3 + \eta)h - 6(\beta^2 - \eta)(-1+\eta)h^2 \\
&+4(-1+\eta)(\beta + \eta)h^3 + (-1+\eta)^2 h^4),
\end{aligned}$$

$$\begin{aligned}
\frac{\mathrm{d}p_2}{\mathrm{d}x} = &((\beta - h)(6(1+\beta)\eta(\beta - h)(1+h)q B_1' \\
&- B_1(\varepsilon_1(\beta - h)(\beta^2 + 3\eta + 4\beta\eta + 2(\eta + \beta(-1+2\eta))h - (-1+\eta)h^2)B_1' \\
&+6(1+\beta)\eta(1+h)qh') + (\beta - h)(\beta^2 + 3\eta + 4\beta\eta + 2(\eta + \beta(-1+2\eta))h \\
&-(-1+\eta)h^2)(\varepsilon_2 B_2 B_2' - h'''))) / (\beta^4 + 4\beta\eta + 6\beta^2\eta + 4\beta^3\eta + \eta^2 \\
&+4(-1+\eta)(\beta^3 + \eta)h - 6(\beta^2 - \eta)(-1+\eta)h^2 \\
&+4(-1+\eta)(\beta + \eta)h^3 + (-1+\eta)^2 h^4).
\end{aligned}$$

In all of these expressions, primes (′) denote differentiation with respect to x.

A.2. *Base-state charge details*

Below is the full expression for the base-state charge expression:

$$\bar{q}(t) = D_1 + D_2 \left[D_3 \exp(-D_6 t) + D_4 \sin(\omega t) - D_5 \cos(\omega t) \right],$$

$$D_1 = \frac{(AC - 1)(S_1\varepsilon_2 - S_2\varepsilon_2)}{S_1 + S_2\beta},$$

$$D_2 = \frac{1}{(S_1 + S_2\beta)^2 + \omega^2(\varepsilon_1 + \varepsilon_2\beta)^2},$$

$$D_3 = \frac{(S_1\varepsilon_2 - S_2\varepsilon_1)((S_1 + S_2\beta)^2 + (1 - AC)\omega^2(\varepsilon_1 + \varepsilon_2\beta)^2)}{S_1 + S_2\beta},$$

$$D_4 = AC(S_2\varepsilon_1 - S_1\varepsilon_2)(\varepsilon_1 + \varepsilon_2\beta)\omega,$$

$$D_5 = -AC(S_2\varepsilon_1 - S_1\varepsilon_2)(S_1 + S_2\beta),$$
$$D_6 = \frac{S_1 + S_2\beta}{\varepsilon_1 + \varepsilon_2\beta}.$$

A.3. *Linear evolution equation details*

Below are the constants from the linear evolution equations (2.26)–(2.27):

$$C_1 = \frac{\beta^2}{6(\varepsilon_1 + \beta\varepsilon_2)^3(\beta^4 + 4\beta\eta + 6\beta^2\eta + 4\beta^3\eta + \eta^2)},$$

$$C_2 = 2\beta(\varepsilon_1 + \beta\varepsilon_2)^3(\beta + \eta),$$

$$C_3 = -\beta^4\varepsilon_1\varepsilon_2 - 3\beta^5\varepsilon_2^2 - 3\varepsilon_1^2\eta - \beta\varepsilon_1\varepsilon_2\eta + \beta^3\varepsilon_2(3\varepsilon_2\eta + \varepsilon_1(7 + 2\eta))$$
$$+ \beta^2\varepsilon_1(3\varepsilon_1 + \varepsilon_2(2 + 7\eta)),$$

$$C_4 = (1 + \beta)\varepsilon_1\varepsilon_2(-\beta^2(\varepsilon_1 - 4\varepsilon_2) + 3\beta^3\varepsilon_2 - 3\varepsilon_1\eta + \beta(-4\varepsilon_1 + \varepsilon_2)\eta),$$

$$C_5 = 2\varepsilon_1\beta(\varepsilon_1 - \varepsilon_2)^2\varepsilon_2(\beta + \eta),$$

$$C_6 = (\varepsilon_1 + \beta\varepsilon_2)\beta(5\beta^3\varepsilon_2 - 5\varepsilon_1\eta + \beta^2(3\varepsilon_1 + 2\varepsilon_2\eta) - \beta(2\varepsilon_1 + 3\varepsilon_2\eta)),$$

$$C_7 = 2\beta(1 + \beta)\varepsilon_1\varepsilon_2(\varepsilon_1 + \beta\varepsilon_2)(\beta + \eta),$$

$$C_8 = 3\left(-4\beta^4\varepsilon_1\varepsilon_2 + \beta^5\varepsilon_1\varepsilon_2 + 2\beta^6\varepsilon_2^2 - 2\varepsilon_1^2\eta - \beta\varepsilon_1\varepsilon_2\eta + 4\beta^2\varepsilon_1\varepsilon_2\eta\right.$$
$$\left. + \beta^3\left(-2\varepsilon_1^2 + \varepsilon_1\varepsilon_2(-1 + \eta) + 2\varepsilon_2^2\eta\right)\right)/\beta,$$

$$C_9 = 3(\varepsilon_1 + \beta\varepsilon_2)^3(\beta^2 - \eta),$$

$$C_{10} = \frac{(1 + \beta)(S_2\varepsilon_1 - S_1\varepsilon_2)}{(\varepsilon_1 + \beta\varepsilon_2)^2}$$

$$C_{11} = 3\varepsilon_1\varepsilon_2(\varepsilon_1 - \varepsilon_2)^2(\beta^2 - \eta),$$

$$C_{12} = 6(1 + \beta)^2\varepsilon_1\varepsilon_2(\beta^3\varepsilon_2 + \varepsilon_1\eta)/\beta,$$

$$C_{13} = \frac{(S_2\varepsilon_1 - S_1\varepsilon_2)(\varepsilon_2 - \varepsilon_1)}{(\varepsilon_1 + \beta\varepsilon_2)^2},$$

$$C_{14} = \frac{S_1 + \beta S_2}{\varepsilon_1 + \beta\varepsilon_2},$$

$$C_{15} = 3(\varepsilon_1 + \beta\varepsilon_2)(2\beta^3\varepsilon_1 + 3\beta^4\varepsilon_2 + 3\varepsilon_1\eta + 2\beta\varepsilon_2\eta - \beta^2(\varepsilon_1 + \eta\varepsilon_2)),$$

$$C_{16} = 3(1 + \beta)\varepsilon_1\varepsilon_2(\varepsilon_1 + \beta\varepsilon_2)(\beta^2 - \eta).$$

A.4. *Floquet matrix details*

Below are the constants from the Floquet evolution equation expansions (4.2)–(4.3):

$$G_1^0 = \tfrac{1}{2}C_1\left((2 - 4AC + 3AC^2)C_5 - C_4(2(-1 + AC)D_1 + AC D_2 D_5)\right.$$
$$\left. + C_3\left(2D_1^2 + D_2^2\left(D_4^2 + D_5^2\right)\right)\right)k^2 - C_1 C_2 k^4,$$

$$G_1^1 = -\tfrac{1}{2}C_1(2AC^2C_5 + (C_4 + 2C_3 D_1)D_2(iD_4 + D_5)$$
$$- AC(2C_5 + C_4(D_1 + iD_2 D_4 + D_2 D_5)))k^2,$$

$$G_1^2 = \tfrac{1}{4}C_1\left(AC^2C_5 + AC C_4 D_2(-iD_4 - D_5) - C_3 D_2^2(D_4 - iD_5)^2\right)k^2,$$

$$G_1^3 = 0,$$

$$G_2^0 = -C_1((-1 + AC)C_7 + C_6 D_1)k^2,$$

$$G_2^1 = \tfrac{1}{2}C_1(AC C_7 + C_6 D_2(iD_4 + D_5))k^2,$$

$$G_2^2 = 0,$$

$$G_2^3 = 0,$$

$$G_3^0 = C_{13} - AC\,C_{13} + C_1 D_1 + \tfrac{1}{2}C_1\big(C_{11}\big((2 - 4AC + 3AC^2)D_1$$
$$+ 2(-1 + AC)AC\,D_2 D_5\big) - C_8 D_1\big(2D_1^2 + 3D_2^2\big(D_4^2 + D_5^2\big)\big) - C_{12}(2(-1 + AC)D_1^2$$
$$+ 2AC\,D_1 D_2 D_5 + (-1 + AC)D_2^2\big(D_4^2 + D_5^2\big)\big)\big)k^2 - C_1 C_9 D_1 k^4,$$

$$G_3^1 = \tfrac{1}{8}(4AC\,C_{13} - 4C_1 D_2(\mathrm{i}D_4 + D_5)) + \tfrac{1}{8}C_1\big(-AC^2 C_{11}(8D_1 + 5\mathrm{i}D_2 D_4 + 7D_2 D_5)$$
$$+ D_2(\mathrm{i}D_4 + D_5)\big(-4C_{11} - 8C_{12}D_1 + 3C_8\big(4D_1^2 + D_2^2\big(D_4^2 + D_5^2\big)\big)\big)$$
$$+ AC\big(8C_{11}(D_1 + D_2(\mathrm{i}D_4 + D_5))$$
$$+ C_{12}\big(4D_1^2 + 8D_1 D_2(\mathrm{i}D_4 + D_5) + D_2^2\big(D_4^2 + 2\mathrm{i}D_4 D_5 + 3D_5^2\big)\big)\big)\big)k^2$$
$$+ \tfrac{1}{2}C_1 C_9 D_2(\mathrm{i}D_4 + D_5)k^4,$$

$$G_3^2 = \tfrac{1}{4}C_1\big(-(C_{12} - 3C_8 D_1)D_2^2(D_4 - \mathrm{i}D_5)^2 + AC^2 C_{11}(D_1 + 2D_2(\mathrm{i}D_4 + D_5))$$
$$- \mathrm{i}AC\,D_2(D_4 - \mathrm{i}D_5)(2C_{11} + C_{12}(2D_1 + D_2(\mathrm{i}D_4 + D_5)))\big)k^2,$$

$$G_3^3 = -\tfrac{1}{8}\mathrm{i}C_1 D_2(AC^2 C_{11} + AC\,C_{12}D_2(-\mathrm{i}D_4 - D_5) + C_8 D_2^2(D_4 - \mathrm{i}D_5)^2)(D_4 - \mathrm{i}D_5)k^2,$$

$$G_4^0 = -C_{14} - \tfrac{1}{2}C_1(C_{16}(2(-1 + AC)D_1 + AC\,D_2 D_5) + C_{15}\big(2D_1^2 + D_2^2\big(D_4^2 + D_5^2\big)\big))k^2,$$

$$G_4^1 = \tfrac{1}{2}C_1(-\mathrm{i}(C_{16} - 2C_{15}D_1)D_2(D_4 - \mathrm{i}D_5) + AC\,C_{16}(D_1 + D_2(\mathrm{i}D_4 + D_5)))k^2,$$

$$G_4^2 = \tfrac{1}{4}C_1 D_2(-\mathrm{i}AC\,C_{16} + C_{15}D_2(D_4 - \mathrm{i}D_5))(D_4 - \mathrm{i}D_5)k^2,$$

$$G_4^3 = 0.$$

REFERENCES

ASSENDER, H., BLIZNYUK, V. & PORFYRAKIS, K. 2002 How surface topography relates to materials' properties. *Science* **297** (5583), 973–976.

BANDYOPADHYAY, D. & SHARMA, A. 2007 Electric field induced instabilities in thin confined bilayers. *J. Colloid Interface Sci.* **311** (2), 595–608.

BENJAMIN, T. B. & URSELL, F. 1954 The stability of the plane free surface of a liquid in vertical periodic motion. *Proc. R. Soc. London, Ser. A* **225**, 505–515.

BRENAN, K. E., CAMPBELL, S. L. V. & PETZOLD, L. R. 1996 Numerical Solution of Initial Value Problems in Differential-Algebraic Equations. *SIAM Classics Series*.

BRISKMAN, V. A. & SHAIDUROV, G. F. 1968 Parametric instability of a fluid surface in an alternating electric field. *Dokl. Akad. Nauk* **13** (6), 540–542.

CHOU, S. Y. & ZHUANG, L. 1999 Lithographically induced self-assembly of periodic polymer micropillar arrays. *J. Vac. Sci. Technol.,* B **17** (6), 3197–3202.

CHOU, S. Y., ZHUANG, L. & GUO, L. 1999 Lithographically induced self-construction of polymer microstructures for resistless patterning. *Appl. Phys. Lett.* **75** (7), 1004–1006.

CONTI, M., DONATI, G., CIANCIOLO, G., STEFONI, S. & SAMOR, B. 2002 Force spectroscopy study of the adhesion of plasma proteins to the surface of a dialysis membrane: role of the nanoscale surface hydrophobicity and topography. *J. Biomed. Mater. Res.* **61** (3), 370–379.

CRASTER, R. V. & MATAR, O. K. 2005 Electrically induced pattern formation in thin leaky dielectric films. *Phys. Fluids* **17** (3), 032104.

CURTIS, A. & WILKINSON, C. 1997 Topographical control of cells. *Biomaterials* **18** (24), 1573–1583.

DEARO, J. A., WESTON, K. D., BURATTO, S. K. & LEMMER, U. 1997 Mesoscale optical properties of conjugated polymers probed by near-field scanning optical microscopy. *Chem. Phys. Lett.* **277** (5–6), 532–538.

DELCAMPO, A., LVAREZ, I., FILIPE, S. & WILHELM, M. 2007 3D microstructured surfaces obtained by soft-lithography using fast-crosslinking elastomeric precursors and 2d masters. *Adv. Funct. Mater.* **17** (17), 3590–3597.

DESHPANDE, P., PEASE, L. F., CHEN, L., CHOU, S. Y. & RUSSEL, W. B. 2004 Cylindrically symmetric electrohydrodynamic patterning. *Phys. Rev.* E **70** (4), 041601.

DEVITT, E. B. & MELCHER, J. R. 1965 Surface electrohydrodynamics with high-frequency fields. *Phys. Fluids* **8** (6), 1193–1195.

DICKEY, M. D., GUPTA, S., LEACH, K. A., COLLISTER, E., WILLSON, C. G. & RUSSELL, T. P. 2006 Novel 3-d structures in polymer films by coupling external and internal fields. *Langmuir* **22** (9), 4315–4318.

DICKEY, M., RAINES, A., COLLISTER, E., BONNECAZE, R., SREENIVASAN, S. & WILLSON, C. 2007 High-aspect ratio polymeric pillar arrays formed via electrohydrodynamic patterning. *J. Mater. Sci.* **43** (1), 117–122.

EDWARDS, W. S. & FAUVE, S. 1994 Patterns and quasi-patterns in the faraday experiment. *J. Fluid Mech.* **278**, 123–148.

FARADAY, M. 1831 On a peculiar class of acoustical figures; and on certain forms assumed by groups of particles upon vibrating elastic surfaces. *Phil. Trans. R. Soc. Lond.* **121**, 299–340.

GONZÁLEZ, H., CASTELLANOS, A., BARRERO, A. & MCCLUSKEY, F. M. J. 1989 Stabilization of dielectric liquid bridges by electric fields in the absence of gravity. *J. Fluid Mech.* **206**, 545–561.

GONZÁLEZ, H., GARCIA, F. J. & CASTELLANOS, A. 2003 Stability analysis of conducting jets under ac radial electric fields for arbitrary viscosity. *Phys. Fluids* **15** (2), 395–407.

GONZÁLEZ, H., RAMOS, A. & CASTELLANOS, A. 1997 Parametric instability of dielectric, slightly viscous liquid jets under ac electric fields. *Phys. Fluids* **9** (6), 1830–1837.

GONZÁLEZ, H., RAMOS, A. & CASTELLANOS, A. 1999 Parametric instability of conducting, slightly viscous liquid jets under periodic electric fields. *J. Electrostat.* **47** (1–2), 27–38.

HARRISON, C., STAFFORD, C. M., ZHANG, W. & KARIM, A. 2004 Sinusoidal phase grating created by a tunably buckled surface. *Appl. Phys. Lett.* **85** (18), 4016–4018.

KIM, D. & LU, W. 2006 Three-dimensional model of electrostatically induced pattern formation in thin polymer films. *Phys. Rev.* B **73** (3), 035206.

KUMAR, K. & BAJAJ, K. M. S. 1995 Competing patterns in the Faraday experiment. *Phys. Rev.* E **52** (5), R4606–R4609.

LEACH, K. A., GUPTA, S., DICKEY, M. D., WILLSON, C. G. & RUSSELL, T. P. 2005 Electric field and dewetting induced hierarchical structure formation in polymer/polymer/air trilayers. *Chaos* **15** (4), 047506.

LEE, B. S., CHO, H.-J., LEE, J.-G., HUH, N., CHOI, J.-W. & KANG, I. S. 2006a Drop formation via breakup of a liquid bridge in an ac electric field. *J. Colloid Interface Sci.* **302** (1), 294–307.

LEE, S. H., KIM, P., JEONG, H. E. & SUH, K. Y. 2006b Electrically induced formation of uncapped, hollow polymeric microstructures. *J. Micromech. Microengng* **16** (11), 2292–2297.

LEI, X., WU, L., DESHPANDE, P., YU, Z., WU, W., GE, H. & CHOU, S. Y. 2003 100 nm period gratings produced by lithographically induced self-construction. *Nanotechnology* **14** (7), 786–790.

LIN, Z., KERLE, T., BAKER, S. M., HOAGLAND, D. A., SCHAFFER, E., STEINER, U. & RUSSELL, T. P. 2001 Electric field induced instabilities at liquid/liquid interfaces. *J. Chem. Phys.* **114** (5), 2377–2381.

LIN, Z., KERLE, T., RUSSELL, T. P., SCHAFFER, E. & STEINER, U. 2002 Structure formation at the interface of liquid/liquid bilayer in electric field. *Macromolecules* **35** (10), 3971–3976.

MELCHER, J. R. & SMITH, C. V. 1969 Electrohydrodynamic charge relaxation and interfacial perpendicular-field instability. *Phys. Fluids* **12** (4), 778–790.

MELCHER, J. R. & WARREN, E. P. 1966 Continuum feedback control of a Rayleigh–Taylor type instability. *Phys. Fluids* **9** (11), 2085–2094.

MORARIU, M. D., VOICU, N. E., SCHAFFER, E., LIN, Z., RUSSELL, T. P. & STEINER, U. 2003 Hierarchical structure formation and pattern replication induced by an electric field. *Nat. Mater.* **2** (1), 48–52.

NABETANI, Y., YAMASAKI, M., MIURA, A. & TAMAI, N. 2001 Fluorescence dynamics and morphology of electroluminescent polymer in small domains by time-resolved SNOM. *Thin Solid Films* **393** (1–2), 329–333.

PEASE, L. F. & RUSSEL, W. B. 2002 Linear stability analysis of thin leaky dielectric films subjected to electric fields. *J. Non-Newtonian Fluid Mech.* **102** (2), 233–250.

PEASE, L. F. & RUSSEL, W. B. 2003 Electrostatically induced submicron patterning of thin perfect and leaky dielectric films: a generalized linear stability analysis. *J. Chem. Phys.* **118** (8), 3790–3803.

PEASE, L. F. & RUSSEL, W. B. 2004 Limitations on length scales for electrostatically induced submicrometer pillars and holes. *Langmuir* **20** (3), 795–804.

Pease, L. F. & Russel, W. B. 2006 Charge driven, electrohydrodynamic patterning of thin films. *J. Chem. Phys.* **125** (18), 184716.

Ranucci, C. S. & Moghe, P. V. 2001 Substrate microtopography can enhance cell adhesive and migratory responsiveness to matrix ligand density. *J. Biomed. Mater. Res.* **54** (2), 149–161.

Reynolds, J. M. 1965 Stability of an electrostatically supported fluid column. *Phys. Fluids* **8** (1), 161–170.

Roberts, S. A. 2009 Stability of microscale fluid interfaces: a study of fluid flows near soft substrates and pattern formation under electrostatic fields. PhD thesis, University of Minnesota (in preparation).

Robinson, J. A., Bergougnou, M. A., Cairns, W. L., Castle, G. S. P. & Inculet, I. I. 2000 Breakdown of air over a water surface stressed by a perpendicular alternating electric field, in the presence of a dielectric barrier. *IEEE Trans. Ind. Appl.* **36** (1), 68–75.

Robinson, J. A., Bergougnou, M. A., Castle, G. S. P. & Inculet, I. I. 2001 The electric field at a water surface stressed by an AC voltage. *IEEE Trans. Ind. Appl.* **37** (3), 735–742.

Robinson, J. A., Bergougnou, M. A., Castle, G. S. P. & Inculet, I. I. 2002 A nonlinear model of AC-field-induced parametric waves on a water surface. *IEEE Trans. Ind. Appl.* **38** (2), 379–388.

Russel, W. B., Saville, D. A. & Schowalter, W. R. 1989 *Colloidal Dispersions*. Cambridge University Press.

Sato, M. 1984 The production of essentially uniform-sized liquid droplets in gaseous or immiscible liquid media under applied A.C. potential. *J. Electrostat.* **15** (2), 237–247.

Saville, D. A. 1997 Electrohydrodynamics: the Taylor–Melcher leaky dielectric model. *Annu. Rev. Fluid Mech.* **29** (1), 27–64.

Schäffer, E., Thurn-Albrecht, T., Russell, T. P. & Steiner, U. 2000 Electrically induced structure formation and pattern transfer. *Nature* **403** (6772), 874–877.

Schäffer, E., Thurn-Albrecht, T., Russell, T. P. & Steiner, U. 2001 Electrohydrodynamic instabilities in polymer films. *Europhys. Lett.* **53** (4), 518–524.

Shankar, V. & Sharma, A. 2004 Instability of the interface between thin fluid films subjected to electric fields. *J. Colloid Interface Sci.* **274** (1), 294–308.

Taylor, G. I. & McEwan, A. D. 1965 The stability of a horizontal fluid interface in a vertical electric field. *J. Fluid Mech.* **22** (1), 1–15.

Thaokar, R. M. & Kumaran, V. 2005 Electrohydrodynamic instability of the interface between two fluids confined in a channel. *Phys. Fluids* **17** (8), 084104.

Topaz, C. M., Porter, J. & Silber, M. 2004 Multifrequency control of faraday wave patterns. *Phys. Rev.* E **70** (6), 066206.

Tsai, I. Y., Kimura, M., Stockton, R., Green, J. A., Puig, R., Jacobson, B. & Russell, T. P. 2004 Fibroblast adhesion to micro- and nano-heterogeneous topography using diblock copolymers and homopolymers. *J. Biomed. Mater. Res.* A **71A** (3), 462–469.

Verma, R., Sharma, A., Kargupta, K. & Bhaumik, J. 2005 Electric field induced instability and pattern formation in thin liquid films. *Langmuir* **21** (8), 3710–3721.

Voicu, N. E., Harkema, S. & Steiner, U. 2006 Electric-field-induced pattern morphologies in thin liquid films. *Adv. Funct. Mater.* **16** (7), 926–934.

Voicu, N. E., Saifullah, M. S. M., Subramanian, K. R. V., Welland, M. E. & Steiner, U. 2007 TiO2 patterning using electro-hydrodynamic lithography. *Soft Matter.* **3**, 554–557.

Wu, L. & Chou, S. Y. 2003 Dynamic modelling and scaling of nanostructure formation in the lithographically induced self-assembly and self-construction. *Appl. Phys. Lett.* **82** (19), 3200–3202.

Wu, N., Pease, L. F. & Russel, W. B. 2005 Electric-field-induced patterns in thin polymer films: weakly nonlinear and fully nonlinear evolution. *Langmuir* **21** (26), 12290–12302.

Wu, N. & Russel, W. B. 2005 Dynamics of the formation of polymeric microstructures induced by electrohydrodynamic instability. *Appl. Phys. Lett.* **86** (24), 241912.

Yeo, L. Y., Lastochkin, D., Wang, S.-C. & Chang, H.-C. 2004 A new AC electrospray mechanism by Maxwell–Wagner polarization and capillary resonance. *Phys. Rev. Lett.* **92** (13), 133902.

Yih, C.-S. 1968 Stability of a horizontal fluid interface in a periodic vertical electric field. *Phys. Fluids* **11** (7), 1447–1449.